

Superconducting NbN-based ultrafast hot-electron single-photon detector for infrared range

A. Verevkin, Y. Xu, X. Zheng, C. Williams, and Roman Sobolewski

Department of Electrical and Computer Engineering and Laboratory of Laser Energetics

University of Rochester, Rochester, NY 14627-0231, USA

O. Okunev, K. Smirnov, G. Chulkova, A. Korneev, A. Lipatov, and G. N. Gol'tsman

Department of Physics, Moscow State Pedagogical University, Moscow 119435, Russia.

Abstract: *Single-photon detector (SPD) with GHz counting rate for infrared range, based on the supercurrent-assisted hotspot effect in a superconducting NbN thin-film microstructure has been developed. A photon-induced hotspot leads to temporary formation of a resistive barrier across the narrow superconducting sensor stripe and results in an easily measurable voltage pulse. Subsequent hotspot healing in <100 ps time frame, restores the superconductivity (zero-voltage state), and the detector is ready to register another photon. It exhibits an experimentally measured intrinsic quantum efficiency up to ~20% and negligible dark counts. Spectral dependence of the photoresponse is presented.*

I. Introduction

Single-photon detection is the ultimate sensitivity limit on any radiation detector. While single-photon detectors (SPD) for the x-ray to the visible photon counting are currently commonplace using photomultiplier tubes¹ or quantum semiconductor avalanche photodiodes², detection of single infrared photons remains a major technological challenge because infrared photons carry significantly less energy than those of visible light, making it difficult to engineer an efficient electron cascade. The most successful silicon avalanche photodiodes have a spectral sensitivity limited to below 1 μm , restricted by the Si bandgap, while photodiodes based on narrow-gap semiconductors currently exhibit unacceptably large dark counts. Vacuum photomultipliers are bulky and have extremely low quantum efficiency for above-1- μm -wavelength photons. Finally,

the most recently proposed far-infrared detectors based on single-electron transistors³ are slow and require millikelvin temperatures and tesla-level magnetic fields. New superconducting devices are the natural choice for fast and ultrasensitive infrared detection, because of their quantum nature and low-noise cryogenic operation environment. The superconducting energy gap 2Δ is two to three orders of magnitude lower than in a semiconductor; thus, the photon absorption in a superconducting detector creates an avalanche electron charge two to three orders of magnitude higher for the same photon energy. This results in an enhanced resolution in energy-resolving devices, such as superconducting tunnel junctions^{4,5}, and extends the range of detectable energies well into the infrared range for photodetectors⁶. In addition, as we have recently demonstrated, energy relaxation time constants of excited electrons in superconductors are in the picosecond range for both the low-temperature⁷ and high-temperature⁸ superconductors, assuring the gigahertz repetition rate for superconducting photon counters.

We have developed simple to manufacture, easy to operate, superconducting SPD's. The approach that we present is to use the hot-electron photoresponse in a superconducting NbN thin-film microstructure with a large active area. This type of device is characterized by a very fast response time (down to ~ 30 ps), high intrinsic quantum efficiency (up to 20%), and negligible dark counts.

The SPD's detection mechanism is based on supercurrent-assisted hotspot formation of a resistive barrier across a very narrow superconducting stripe, kept at the temperature well below the material's superconducting transition $T_c \sim 11$ K for NbN. The hotspot formation process

includes formation of phase-slip-centers (PSC) and results in a large (above 1 mV), easily measurable voltage signal.

II. Device fabrication and geometry

We use nominally 0.1-0.2- μm -wide meandering strip patterned from ultrathin (5-nm-thick) NbN films deposited on sapphire substrate by reactive dc magnetron sputtering in an Ar + N₂ gas mixture⁹. NbN meander type microstructures that cover either 4 μm by 4 μm , or 10 μm by 10 μm active areas were patterned with using of electron beam lithography technique. SEM image of the 4x4 μm area device is presented in Fig. 1. We used short single stripe devices with sizes either 0.1x0.1 μm and 0.2x0.2 μm as well.

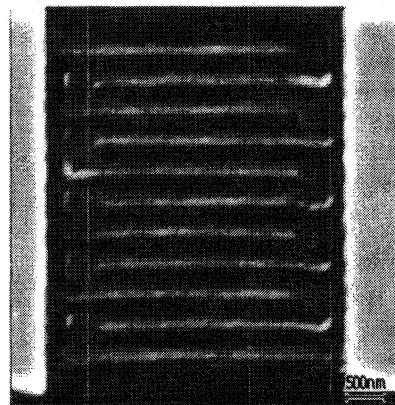


Fig. 1. SEM image of a meander-type SPD structure with 4x4 μm area.

III. Experimental Setup

In our experiments, a NbN SPD was mounted on a cold plate ($T = 4.2$ K) inside an optical cryostat. We used two cold glass filters to block the room temperature background radiation falling on the sample. The sample was dc biased and mounted on a rigid coplanar transmission line with the ac output connected to a cryogenic low-noise

amplifier with the input cryogenic isolator, characterized by 30-dB gain and 1-2 GHz

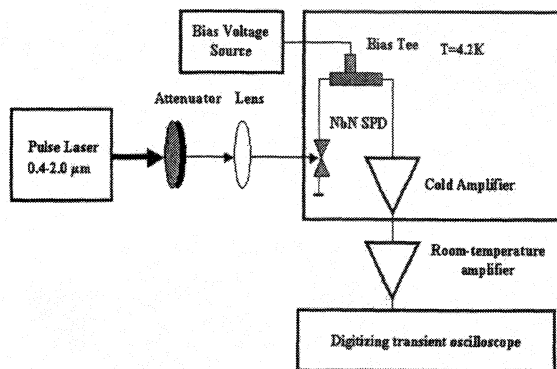


Fig. 2. Experimental Setup.

bandwidth (Fig. 2). Outside the dewar, the signal passed through a second broadband power amplifier (9 GHz; 20-dB gain) before going to a 6-GHz or 12 GHz-bandwidth single-shot oscilloscopes for display and then to a 200-MHz voltage-level threshold counter for real-time event counting and statistical analysis. We worked with 100-fs-wide optical pulses with a 1-kHz repetition rate at 0.4 μm , 0.81 μm , 1.55 μm , and 2.1 μm wavelengths. The intensity of the laser pulses was attenuated using banks of neutral density filters. The diameter of the beam incident on the device was $\sim 50 \mu\text{m}$. Wavelength dependencies of quantum efficiency were measured using grating spectrometer, or interferometric filters, and CW radiation source.

IV. Experimental Results and Discussion.

The current-voltage (I - V) characteristics of a NbN $0.2 \times 0.2 \mu\text{m}^2$ microbridge, operated at 4.2 K, is shown in Fig. 3.

The device is normally biased in the superconducting (zero-resistance) state. The dashed-line section of the resistive characteristics corresponds to the metastable region (which cannot be accessed under dc operating conditions) when the device is connected to a 50Ω load of the output coaxial line, biased below its critical current I_C , and no light is incident upon the microbridge. The device I_C typically is within range of 40-120 μA , while the normal-state resistance is equal to 300-500 Ω for 0.2×0.2 and $0.1 \times 0.1 \mu\text{m}^2$ single strip devices, and 50-70 k Ω for meander type $10 \times 10 \mu\text{m}$ device. For a device biased near, but below I_C , photon absorption leads to a temporary switch from the stable superconducting state (point A in Fig. 3) to the sub-critical resistive state (point B in Fig. 3). As a result, we observe a voltage pulse whose amplitude corresponds to the voltage level at point B, and time duration that depends on the dynamics of formation and subsequent healing of the resistive state induced by the photon absorption. This process is reversible due to the metastable character of the sub-critical state.

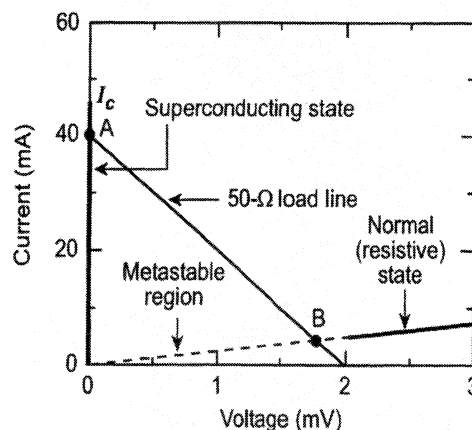


Fig. 3. I-V curve of SPD.

The dynamics of the hotspot formation in a superconductor at

temperature T below its critical temperature T_c , has been described before¹⁰ and studied in details in Ref.11. Absorption of a photon with energy $\hbar\omega \gg 2\Delta$ creates, through electron–electron and electron–Debye-phonon interactions, a local nonequilibrium perturbation with a large number of excited hot electrons (above 300 for NbN, excited with 800-nm wavelength light⁶), and an increase of the average electron temperature above T_c . This initial phase is called the thermalization process and for ultrathin NbN films is characterized by the thermalization time $\tau_T = 6.5 \text{ ps}$ ⁷. The thermalization process results in the formation of a hotspot—a local nonsuperconducting region (Fig. 4a). After the initial thermalization, the resistive hotspot size grows (Fig. 4b) as hot electrons diffuse out of its hotspot region. At the same time, the supercurrent is expelled from its hotspot volume and is concentrated in the “sidewalks” between the hotspot and the edges of the film (Fig. 4c). The microbridge, however, still shows no resistance, unless the bias current I_{bias} is sufficient to exceed the critical current in the sidewalks. In this latter case, superconductivity in the sidewalks is destroyed, and the resistive barrier is formed across the entire width w of the device (Fig. 4d), giving rise to a voltage signal with amplitude proportional to the barrier resistance. Resistance of normal areas is determined by the length of PCS appeared in sidewalk areas, which is close to double charge-imbalance length. From the other hand charge imbalance length is determined by the inelastic scattering length, which is close to characteristic electron-phonon length in NbN⁷. As the result, each the resistive area in NbN SPD has the length of an electron-phonon length. The normal resistance areas formation process competes, with the cooling process, as electrons diffusing out the hotspot lose their energy

through electron–phonon scattering. Thus, after the time depending on both the diffusion rate and the quasiparticle relaxation dynamics,⁶ the hotspot heals itself, leading to the restoration of the superconducting path along the microbridge.

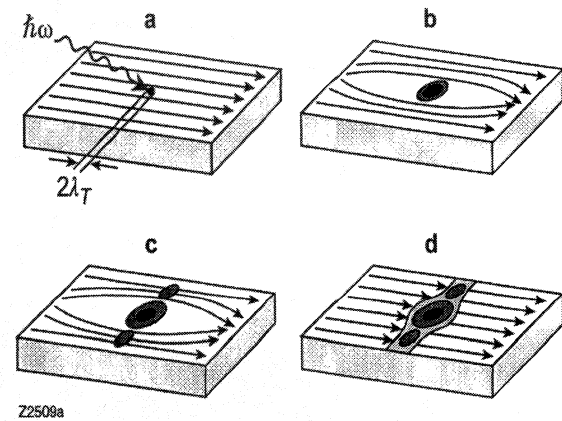


Fig.4. Schematics of a supercurrent-assisted hotspot formation mechanism in an ultrathin and narrow superconducting stripe.

As a result of the hotspot creation and relaxation processes, the device switches temporarily between the superconducting and resistive states (points A and B in Fig. 3) and a voltage pulse is generated at the device terminals. The physical difference between our current-assisted single-photon detection mechanism and an earlier proposed hotspot mechanism¹⁰ is that our response is due to a collaborative effect of the bias current and the radiation quantum, leading to a comparably large, easily measurable output voltage signal. We note that the current-assisted hotspot process creates a nonlinear, multidimensional space of operating parameters, such as w , I_{bias} , $\hbar\omega$, and T .

The time-resolved response of our SPD is shown in Fig. 5. The signal has a pulse width of below 100 ps, with the signal-to-background-noise ratio of above 100:1, and shot-to-shot jitter of less than 30 ps. The measured bandwidth of the output

pulse was limited by the bandwidth of our chain of output amplifiers and the oscilloscope bandwidth. With the proper bandwidth of the output data acquisition system, it is possible to reach the intrinsic

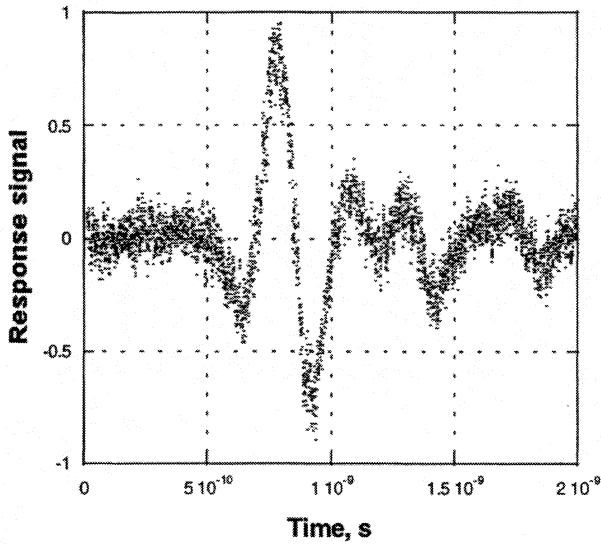
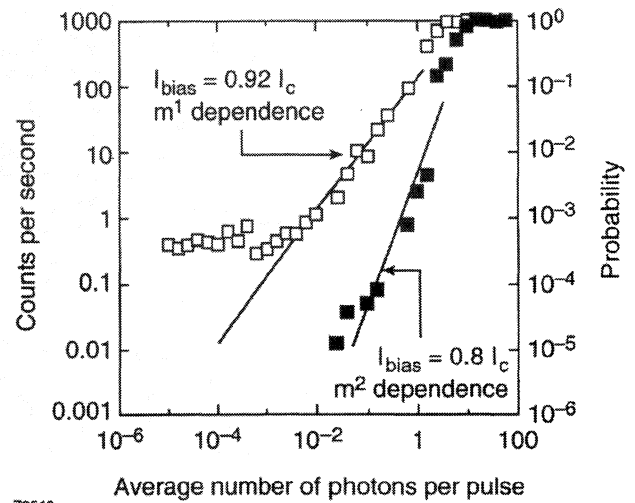


Fig. 5. Time-resolved SPD response.

Truly single-photon counting requires that the photon detection probability is a linear function of the number of photons incident on the device. For a mean number of $m \ll 1$ photons per pulse (far below detector saturation), the probability $P(n)$ of absorbing n photons from a given pulse is proportional to

$$P(n) \sim \frac{m^n}{n!}. \quad (1)$$

Consequently, the probability of absorbing one photon is proportional to m , the probability of detecting two photons is proportional to m^2 , the probability of detecting three photons is proportional to m^3 , and so on.



Z2513

Fig. 6. Counting rate and probability vs. average number of photons per pulse ($0.2 \times 0.2 \mu\text{m}$ device).

Figure 6 shows the probability of the detector producing an output voltage pulse as a function of the average number of photons per pulse, incident on the device area for two different values of I_{bias} . The left vertical axis in Fig. 6 indicates the number of detector counts per second (equivalently, per 1000 laser pulses), based on the average number of counts detected by SPD over a 10-s counting period for the highest photon doses, and up to 1000 s for the lowest. The right vertical axis corresponds to the count rate, probability of detecting an optical pulse. Open squares correspond to the SPD performance when it was biased at $0.92 I_c$.

There is saturation at high incident photon fluxes, but for smaller fluxes, the experimental data show the linear decrease of detection probability versus the average number of incident photons over four orders of magnitude, which unambiguously demonstrates the single-photon detection. At very low photon doses, our experimental data points leveled off at 0.4 counts/sec, which must be regarded as the laboratory

photon background noise. The intrinsic dark count rate of our SPD was below 0.001 counts/sec, which corresponds to the number of detector responses over the time of 1000 sec when its input was completely blocked. The above limit was set by the long-term stability of our dc biasing box. We strongly believe that the intrinsic dark count of our device is significantly lower and should be limited by electron thermal fluctuations. The system noise temperature of our SPD, including the cryogenic amplifier, is below 15 K, which yields to voltage fluctuations several orders of magnitude below our signal levels. From Fig. 6, we can estimate that the quantum efficiency (QE) of our NbN microbridge device is 20%, as the value corresponding to the probability of detecting a pulse containing an average of one photon incident upon the device. The practical detection efficiency of our SPD is, of course, is determined by S_d/S_{in} ratio of the tested structure. Using proper coupling optics, the incident photon beam could be focused to a diffraction-limited spot size.

The solid squares in Fig. 6 correspond to the same device, operated under the same conditions as those for the open-square data, but with $I_{bias} = 0.8 I_C$. We note immediately that our experimental data points now follow a quadratic dependence of detection probability showing the two-photon detection [see Eq. (1)]. As expected, for a two-photon process its QE is significantly lower than that for the single-photon detection and is approximately equal to 1%. At the same time we do not see the laboratory photon background noise since the probability of two stray photons arriving at the device at the same time (more accurately, within the hotspot-formation/healing process) is negligibly small.

Spectral dependencies of QE for two meander-type devices with $4 \times 4 \mu\text{m}$ area size are presented in Fig. 7. As it can be seen, both dependencies have an exponential character with the same slope.

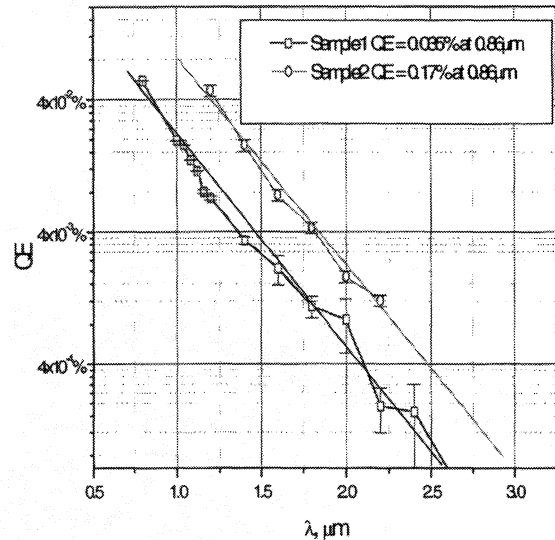


Fig. 7. Spectral dependence of quantum efficiency (meander-type devices).

We have found from our studies of AFM images of devices that the absolute QE values are in good correlation with the nonuniformity level of superconducting stripe edges. An origin of exponential behavior of the QE (λ) needs in future studies.

In conclusion, we have demonstrated that a supercurrent-assisted, hot-spot-formation mechanism can be implemented in ultrathin NbN stripes for ultrafast single-photon detection and counting of visible and infrared photons with experimentally measured quantum efficiency up to 20% and negligible dark counts. The bandwidth-limited measured response time was ~ 100 ps, corresponding to a 10-GHz photon counting rate. Already identified

applications for our superconducting SPD's range from sensing ultraweak electroluminescence from submicron complementary metal-oxide-semiconductor VLSI circuits¹³, to NASA high-data-rate and data-capacity free-space optical communication systems for planetary exploration and earth-orbiting missions¹⁴. Our devices are also envisioned to be the heart of quantum communication systems, which allow for the implementation of unconditionally secure quantum key distribution for high-speed, real-time Vernam enciphering of large volumes of data¹⁵.

We thank Kenneth Wilsher, Steven Kasapi, Seema Somani, and Gerald Gilbert for helpful discussions and comments. This work was supported by Schlumberger TT, US Office of Naval Research under grant N00014-98-1-0080, and the NATO Linkage Grant No. N98062.

References

- ¹ Photomultiplier Tubes, Hamamatsu Photonics K.K.
- ² F. Zappa, A. L. Lacaita, S. D. Cova, and P. Lovati, *Opt. Eng.* **35**, 938 (1996).
- ³ S. Komiyama, O. Astafiev, V. Antonov, T. Kutsuwa, and H. Hirai, *Nature* **403**, 405 (2000).
- ⁴ A. Peacock, P. Verhoeve, N. Rando, A. van Dordrecht, B. G. Taylor, C. Erd, M. A. C. Perryman, R. Venn, J. Howlett, D. J. Goldie, J. Lumley and M. Wallis, *Nature* **381**, 135 (1996).
- ⁵ R. J. Schoelkopf, S. H. Moseley, C. M. Stahle, P. Wahlgren, and P. Delsing, *IEEE Trans. on Appl. Supercond.* **9**, 2935 (1999).
- ⁶ K. S. Il'in, I. I. Milostnaya, A. A. Verevkin, G. N. Gol'tsman, E. M. Gershenzon, and R. Sobolewski, *Appl. Phys. Lett.* **73**, 3938 (1998).
- ⁷ K. S. Il'in, M. Lindgren, M. Currie, A. D. Semenov, G. N. Gol'tsman, R. Sobolewski, S. I. Cherednichenko, and E. M. Gershenzon, *Appl. Phys. Lett.* **76**, 2752 (2000);
- ⁸ M. Lindgren, M. Currie, C. Williams, T. Y. Hsiang, P. M. Fauchet, R. Sobolewski, S. H. Moffat, R. A. Hughes, J. S. Preston, and F. A. Hegmann, *Appl. Phys. Lett.* **74**, 853 (1999).
- ⁹ S. I. Cherednichenko, P. Yagoubov, K. S. Il'in, G. N. Gol'tsman, and E. M. Gershenzon, *Proceedings of the Eighth International Symposium on Space Terahertz Technology* (Harvard University, Cambridge, MA, 1997), pp. 245-252.
- ¹⁰ A. M. Kadin and M. W. Johnson, *Appl. Phys. Lett.* **69**, 3938 (1996).
- ¹¹ A. D. Semenov, G. N. Gol'tsman, and A. Korneev, *Physica C*, in print.
- ¹² M. Born, E. Wolf, *Principles of Optics: Electromagnetic Theory of Propagation, Interference, and Diffraction of Light* (Cambridge University Press, Cambridge, 7th expanded ed., 1999), pp. 752-758.
- ¹³ J. C. Tsang and J. A. Kash, *Appl. Phys. Lett.* **70**, 889 (1997).
- ¹⁴ G. G. Ortiz, J. V. Sandusky, and A. Biswas, in *Free-Space Laser Communication Technologies XII*, edited by G. S. Mercherle, (SPIE, Bellingham, WA, 2000), vol. 3932, pp. 127-138.
- ¹⁵ G. Gilbert and M. Hamrick, MITRE Technical Report, MTR00W0000052